LAWRENCE
LIVERMORE
NATIONAL
LABORATORY

UCRL-PROC-225851

Multilayer defects nucleated by substrate pits: a comparison of actinic inspection and non-actinic inspection techniques

Anton Barty, Kenneth Goldberg, Patrick Kearney, Senajith Rekawa, Bruno LaFontaine, Obert Wood, John S Taylor, Hak-Seung Han

November 3, 2006

SPIE Photomask technology (BACUS)
Monterey, CA, United States
September 18, 2006 through September 22, 2006

Disclaimer

Multilayer defects nucleated by substrate pits: a comparison of actinic inspection and non-actinic inspection techniques

A. Barty[1], K. A. Goldberg[2], P. Kearney[3], S.B.Rekawa[2], B. LaFontaine[4], O. Wood II[3], J.S.Taylor[1] and H.-S. Han[3]

[1] *Lawrence Livermore National Laboratory, P.O. Box 808, Livermore, CA 94550*
[2] *Lawrence Berkeley National Laboratory, 1 Cyclotron Rd, Berkeley, CA 94720*
[3] *SEMATECH, 255 Fuller Road, Suite 309, Albany, NY 12203*
[4] *Advanced Micro Devices, Sunnyvale, CA 94088*

Keywords: EUV mask inspection, EUV reticle, programmed defects

1 Abstract

The production of defect-free mask blanks remains a key challenge for EUV lithography. Mask-blank inspection tools must be able to accurately detect all critical defects whilst simultaneously having the minimum possible false-positive detection rate. We have recently observed and here report the identification of bump-type buried substrate defects, that were below the detection limit of a non-actinic (i.e. non-EUV) inspection tool. Presently, the occurrence of pit-type defects, their printability, and their detectability with actinic techniques and non-actinic commercial tools, has become a significant concern.

We believe that the most successful strategy for the development of effective non-actinic mask inspection tools will involve the careful cross-correlation with actinic inspection and lithographic printing. In this way, the true efficacy of prototype inspection tools now under development can be studied quantitatively against relevant benchmarks. To this end we have developed a dual-mode actinic mask inspection system capable of scanning mask blanks for defects (with simultaneous EUV bright-field and dark-field detection) and imaging those same defects with a zoneplate microscope that matches or exceeds the resolution of EUV steppers.

2 Introduction

A defect is any area on the mask that causes unwanted variations in the aerial image at the wafer plane of a lithographic exposure tool. Defects in the patterned absorber layer consist of regions where absorber material is unintentionally added or removed from the pattern, leading to errors in the reflected field. There currently exists a mature and proven suite of technologies for inspecting and repairing defects in the mask pattern of non-EUVL reticles. However, a problem unique to EUVL is the existence of defects within or below the reflective multilayer coating applied to mask blanks prior to patterning. These defects can perturb the reflected optical field, causing unwanted variations in aerial image contrast, and manifest themselves as defects on printed wafer.

Multilayer reflectivity is a resonant property of the alternating layer structure and is optimized when all the layers interfere constructively satisfying the Bragg condition: a typical multilayer coating for reflecting 13.5-nm wavelength EUV light consists of 40–80 bi-layers of molybdenum and amorphous silicon with each bi-layer consisting of approximately 3-nm Mo and 4-nm Si. Because reflection takes place throughout the bulk of the multilayer, any deformation or disruption of the layer structure can introduce a defect. The goal is to produce multilayers that do not have any defects either on the surface or in the layer structure; however this may be difficult to achieve in practice. It is therefore essential to have strategies for inspecting mask blanks prior to patterning in order to determine whether there are any defects present on the mask blank.

Anticipating that non-actinic tools can and will be used by industry to qualify EUV mask blanks, the study and validation of non-actinic inspection techniques remains a high-priority area of research. The key question to be answered is: Are non-actinic tools *capable* of detecting all printable EUV defects? The physically different responses of EUV and non-EUV tools to multilayer defects is a key issue because of the small size of multilayer defects compared to non-actinic wavelengths, and the different penetration depths into the multilayer bulk structure.

1.1 Wavelength dependence of the light penetration depth

How far light penetrates into the multilayer structure is a particularly important issue for EUV defects. Because of the significant difference in penetration and interaction with the multilayer structure, significant differences can be expected between the signal returned from a multilayer defect at EUV wavelengths and at either the 488-nm or 266-nm wavelengths used in commercial inspection tools. Many authors have shown that even nanometer-scale perturbations of the manufactured resonant multilayer structure can significantly affect local EUV reflectivity; whereas non-actinic wavelengths primarily probe the multilayer surface. This difference in penetration is shown in **Fig. 1**, which shows the field intensity as a function of depth for 13.5-nm EUV light, as well as 488-nm and 266-nm laser light used in current mask inspection tools. Picking the 1% field intensity point for comparison purposes, 13.5-nm EUV light penetrates to 250-nm depth within the multilayer, whereas 488-nm and 266-nm light only penetrate to 52-nm and 20-nm depths respectively before being attenuated to 1% field intensity. The EUV field intensity is resonant with the periodic mirror structure, whereas both 488-nm and 266-nm light show no multilayer resonance effects.

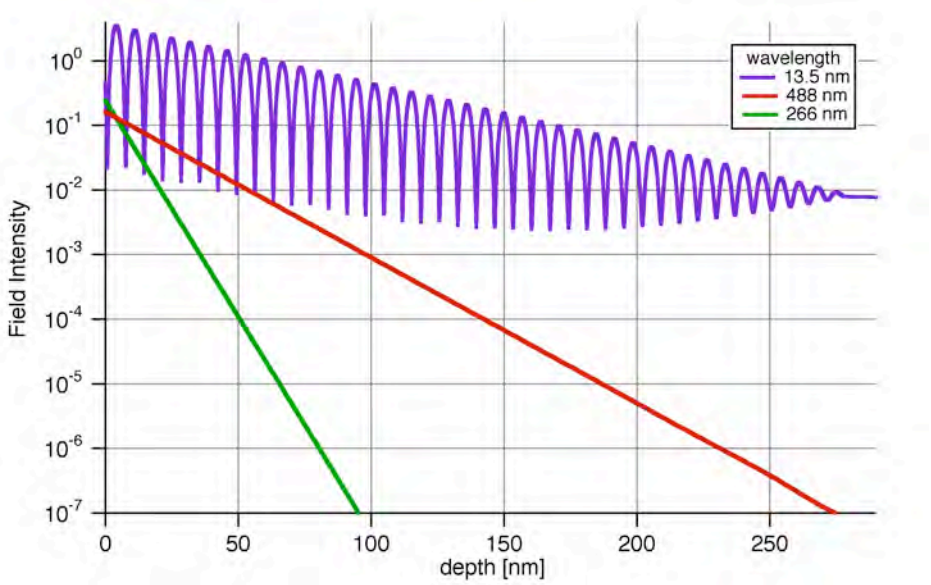

Fig. 1 Field intensity as a function of depth for 13.5-nm wavelength EUV light, as well as 488-nm and 266-nm laser light used in current mask inspection tools. Picking the 1% field intensity point for comparison purposes, 13.5-nm EUV light penetrates to a depth of 250 nm within the multilayer, whereas 488-nm and 266-nm light only penetrate to 52 nm and 20 nm respectively before being attenuated to 1% field intensity.

In this paper we report the cross-comparison of actinic and non-actinic inspection and EUV lithographic printing of a programmed defect mask. The multilayer defects were nucleated by programmed substrate pit defects of varying sizes. We present cross-calibration measurements using an at-wavelength mask inspection system at the Advanced Light Source, Lawrence Berkeley National Laboratory, and compare this to inspection techniques employing non-EUV light made using a commercial laser-based mask inspection system.

3 At-wavelength defect inspection system

At-wavelength inspection of a multilayer-coated programmed defect pit mask was made using a unique at-wavelength mask inspection system located at the Advanced Light Source, Lawrence Berkeley National Laboratory[1,2] . This non-commercial mask inspection system uses synchrotron radiation to inspect EUV masks using monochromatic 13.5-nm illumination. It operates in two complementary inspections modes: *scanning mode* in which both the specular reflection and scattered light signal is recorded as the mask is moved under a stationary 1–5 µm spot; and *imaging mode* in which a zone plate lens is used to project an image of the mask onto an EUV CCD camera for direct recording of aerial images. A picture of the mask inspection system installed at the ALS is shown in **Fig. 2**.

In both modes, a bending-magnet beamline provides illuminates an entrance pinhole; a 20×-demagnification Schwarzschild objective re-images the illuminated pinhole onto the upward-facing reticle with a 6° angle of incidence. During measurement, the beam focus remains stationary in space while the mask is translated and rotated (r, θ) in a manner that allows any position on the mask to be illuminated.

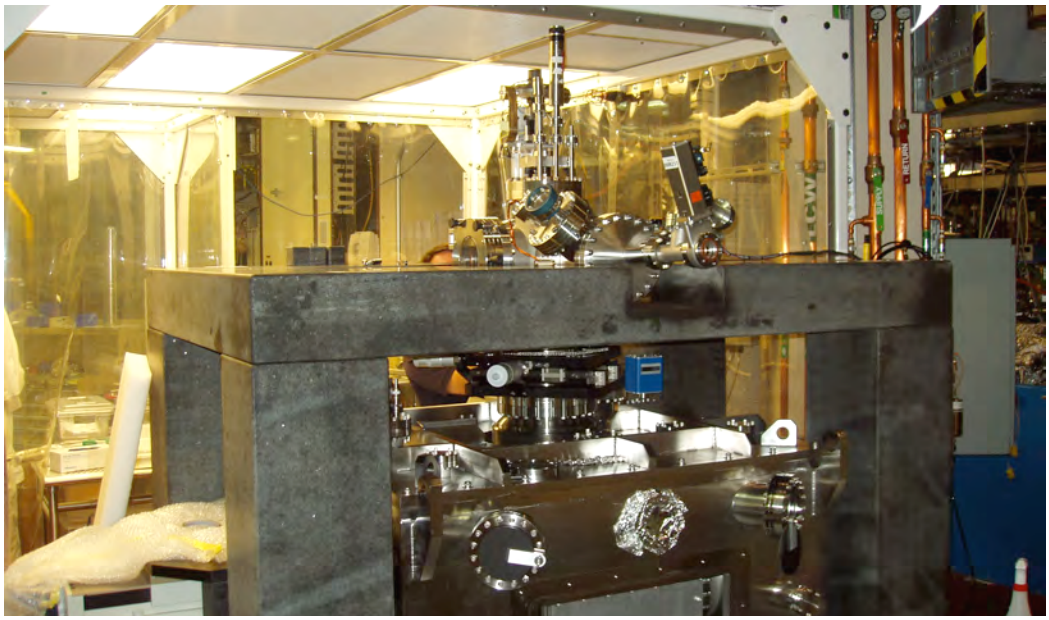

Fig. 2 EUV mask inspection system installed at beamline 11.3.2, Advanced Light Source, Lawrence Berkeley National Laboratory, shown during installation.

2.1 Scanning mode

The mask can be rotated and translated in a manner that allows arbitrary regions to be scanned under the focused beam. Using pinhole apertures with 20 to 100-µm diameters, the beam size on the reticle can be varied from 1 to 5 µm. The beam size relative to the size of defects affects the signal-to-noise ratio (SNR) of the measurements.

The inspection system is flexible in its detector geometry, and is capable of recording brightfield and darkfield signals at up to 100 kHz. The brightfield signal measures local reflectivity changes with 0.1% relative uncertainty. In addition to defect detection, we have demonstrated that the brightfield signal is sensitive to multilayer damage cause by various inspection methods. The darkfield signal records light scattered out of the specular beam by tiny perturbations in the mask. It is especially sensitive to so-called phase-defects.

The inspection data presented here was recorded with a new detector design that records darkfield light in an off-axis angular range of 0.6°–35° from the central ray in one direction, and ±4.3° in the perpendicular direction, and with no intervening mirrors between the mask and the detector. In this way the darkfield detection comes close to the specular beam; the detector was positioned to provide optimal SNR for the defects in this study.

Fig. 3. In scanning mode, the mask is moved under a stationary focal spot of between 1–5 μm size produced by imaging a pinhole onto the mask using 20× reduction Schwarzschild optics. A photodiode placed to intercept the specular reflection measures local reflectivity changes on the mask, whilst a detector positioned to intercept the scattered EUV light records the darkfield signal.

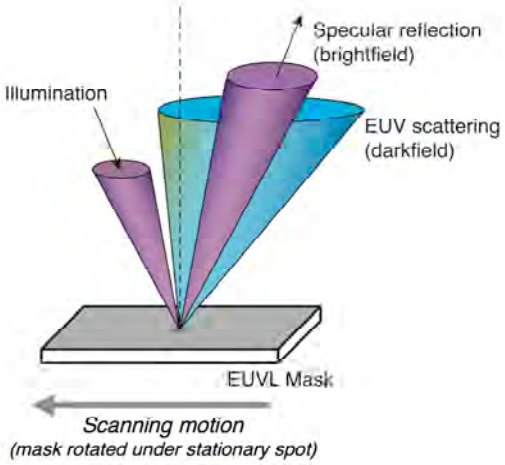

2.2 Imaging mode

The imaging mode subsystem of the EUV mask inspection tool uses a zoneplate lens to produce a real, magnified image of the mask on a CCD camera. In order to properly emulate the imaging characteristics of a 0.25 NA 4×-

reduction lithography stepper it is necessary to have a pupil with a clear aperture of 0.0625 NA observing the mask at an angle of incidence of 6°. In this way the zoneplate sees the mask with the same conditions as the projection optics in a lithographic system.

Equivalence of the through-focus aerial image performance with that of a production system is essential, as many types of defects manifest themselves as changes in the aerial image as a function of focal position. Manufacturing aberrations affect both in-focus and through-focus behavior, and therefore impact the aerial image. A previous design study found that the best way to achieve this equivalence is through the fabrication of a custom EUV optic specifically designed for aerial image measurement[3], and commercial AIM systems with these requirements are in production for use in industry[4]. For the purposes of this project it not justified to construct a custom optic capable of meeting full equivalence with the imaging quality of a stepper optic; however, it is possible to emulate the essential properties of numerical aperture and aberration control at lower cost using a zone plate optic.

Zone plate microscopes typically operate in transmission mode with the condenser and imaging optics on opposite sides of the object. This relies on the object being transparent, whilst EUV masks are reflective. In order to image a reflective EUV mask, it is necessary to fold the system back on itself so that both the illumination and imaging optics are on the same side of the object. The desired mask-side aperture of 0.0625 NA at 6° allows adequate clearance for both the optics and illumination on the same side of the mask, although space is constrained. These issues are similar to accommodating illuminator clearance when designing the mask-side of lithographic optics.

To date, several programmed defect masks have been inspected in imaging mode. More details of the imaging mode operation and performance will be provided in subsequent papers.

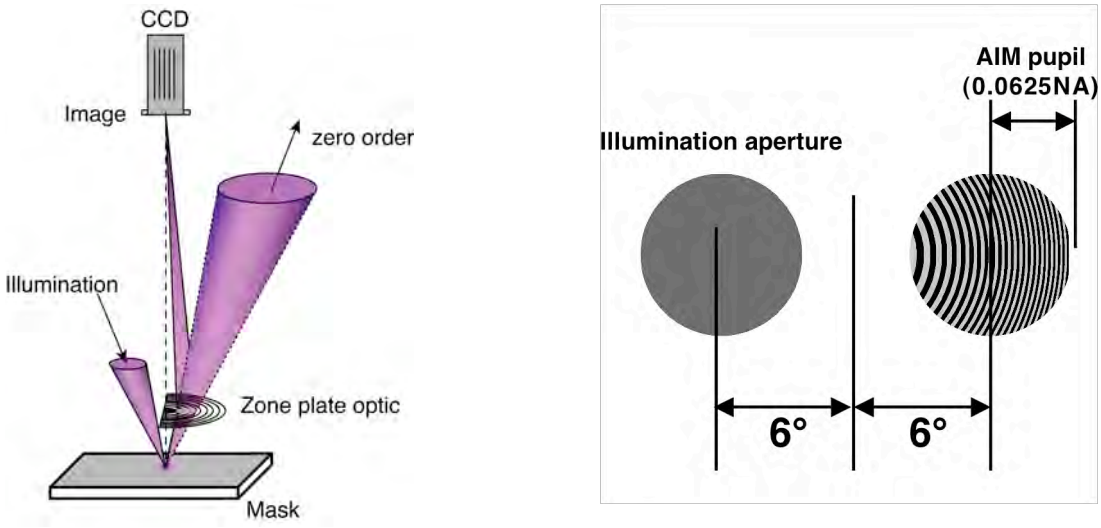

Fig 4: Schematic layout of the zone plate imaging system. An off-axis potion of a 0.166NA parent zone plate is used to image the mask onto the CCD camera, keeping the whole field-of-view in focus and eliminating keystone distortion. To illuminate the mask, only that portion of the zone plate involved in imaging the mask is fabricated – the remainder is left unpatterned and may be used to introduce illumination into the system. Using the off-axis design has the added benefit of physically separating unwanted diffraction orders from the zone plate optic. Due to space constraints within the system, a fold mirror (not shown) is included in our imaging system to project the image onto a CCD to the side of the mask.

4 Programmed defect pit mask

A programmed defect pit mask with an array of pits was fabricated for the purposes of this study. In order to emulate naturally occurring substrate pits, pits were created in a first multilayer coating using a focused ion beam. They were then over-coated with a second multilayer coating to produce a mask with a four regular arrays of pits. The primary reason for using this double-multilayer technique was to obtain higher contrast obtained in the Lasertec M1350 inspection tool than was possible on a bare quartz substrate.

Each of the four arrays was prepared using a different ion-beam current, and within each array different exposure times were used to produce each column of pits. The columns contain ten nominally identical pits to improve the statistical analysis. Pits were produced using ion beam currents in the range of 1–50 pA and exposure times in the range of 1 µsec to 25 sec. The pit widths were 0.2±0.05 µm and their depths range from 2–200 nm. Pre- and post-coating inspection of the pit array in a commercial Lasertec M1350 inspection located that the Mask Blank Development Center in Albany is shown in Fig. 5. Because defects are smoothed in the multilayer coating process, fewer defects are expected to be observed after following multilayer coating of the substrate pits.

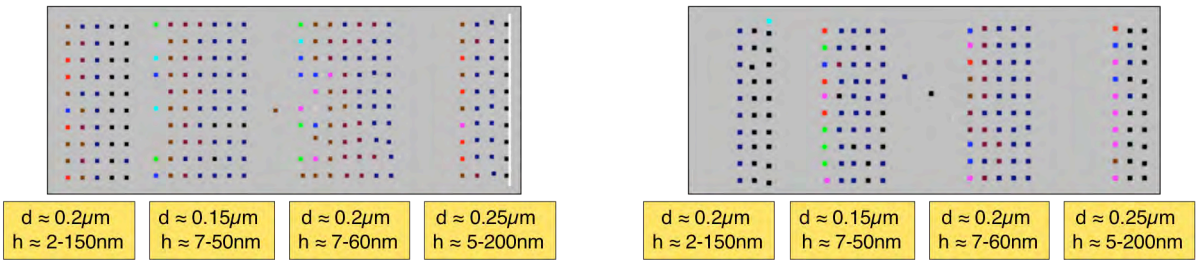

(a) Pre-coating M1350 inspection of the pit array **(b)** Post-coating M1350 inspection of the pit array

Fig. 5 Results of pre-coating **(a)** and post-coating **(b)** inspection of the programmed defect pit array in a commercial Lasertec M1350 inspection tool located at the Mask Blank Development Center in Albany. Defects are smoothed in the multilayer coating process, resulting in fewer defects being observed after multilayer coating of the substrate pits.

5 At-wavelength inspection

At-wavelength inspection of the abovementioned programmed defect pit mask was performed using the Actinic mask inspection system at the Advanced Light Source, Lawrence Berkeley National Laboratory. The system was operated in scanning mode using a 2 µm focal spot on the mask, recording both brightfield and darkfield signals from the same programmed defect array inspected in the non-actinic M1350 multi-beam confocal inspection system using 488-nm wavelength laser light. A complete brightfield scan of the programmed defect array, representing a map of the local mask reflectivity (averaged over the 2 µm focal spot), is shown in Fig. 6, both on a 0-100% color-scale, and an exaggerated color-scale of -4% to +1.5% relative reflectivity range. Note the clear border around the programmed defect region and large fiducial marking in the centre of the array, both of which greatly assist in locating the defect array on an otherwise blank mask surface.

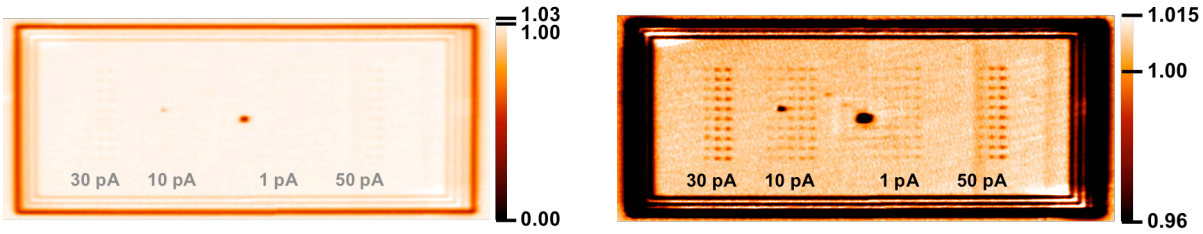

(a) Bright-field scan with standard 0-100% colorscale **(b)** Bright-field scan with exaggerated colorscale

Fig. 6. Actinic brightfield scans of the programmed defect region, measuring the point-by-point reflectivity over the mask surface with a 1 µm spot and an accuracy of ±0.1%, represented with standard **(a)** and exaggerated **(b)** color tables. Note that not only are individual defects visible in the bright-field area scan, but also other forms of damage to the mask itself, particularly the box around the central fiducial, and vertical stripes in the right portion of the image. The border around the programmed defect region and large fiducial marking in the center of the array are used to help locate the defects on the mask surface

Two features in addition to the programmed pit array and fiducials are noticeable in the continuous brightfield scan shown in **Fig. 6**. First, note the 'box' of altered reflectivity visible around the central fiducial region, which we speculate is from SEM imaging whilst the central fiducial was milled using the FIB tool. Second, note the two lines of depressed reflectivity running vertically across the defect region near the 50 pA defect cell; the origin of these marks is unknown, but could be due to either SEM or inspection tool damage during defect review.

Measurement of the defects was made using their known positions to produce single values for EUV brightfield and darkfield signal strengths, as plotted in **Fig. 7**. Here the brightfield signal represents the peak percentage reflectivity loss under the 2.5 µm illuminated spot; the darkfield scattering is a linear scale of representing the signal-to-noise

ratio relative to the background scattered EUV light intensity. Some of the smallest defects did not produce signals above background signal level fluctuations and are represented as open boxes, whilst other defects were too close to strongly scattering native defects to produce a clear signal and are represented by open diamonds.

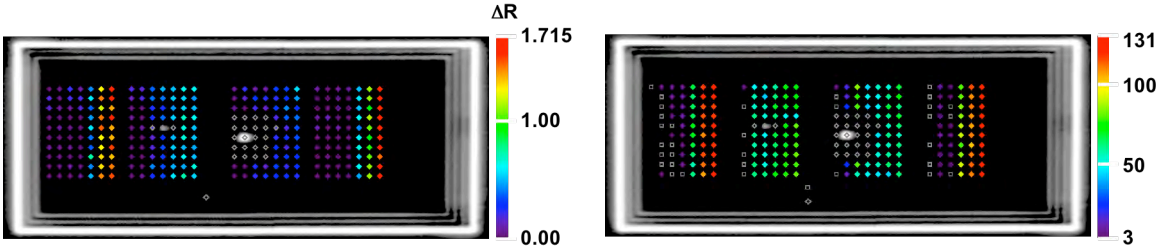

(a) Actinic brightfield defect strength **(b)** Actinic darkfield defect SNR.

Fig. 7 Actinic **(a)** brightfield and **(b)** darkfield inspection results for the programmed defect pit array. Some of the smallest defects did not produce signals above background signal level fluctuations and are represented as open boxes, whilst other defects were too close to strongly scattering native defects to produce a clear signal and are represented by open diamonds.

6 Comparison of actinic and non-actinic inspection results

The first and most obvious comparison to make is between the measured Lasertec M1350 defect size and the actinic brightfield and darkfield scattering measurements. The Lasertec M1350 tool reports size based on two metrics, "pixels" and "bins," and we perform comparisons against both: Fig. 8 shows a comparison of M1350 bin and pixel number against actinic brightfield signal, whist Fig. 9 shows the same Lasertec data plotted against actinic darkfield signal. For the Lasertec inspection system, the defect detection threshold is set high (approximately 7σ) to avoid false positives within the measurement of the entire quality area of a mask under inspection. This choice of detection threshold represents a trade-off between ultimate tool sensitivity and false defect detection rate, and means that some of the programmed defect pits may not have been reported as "defects" even though a detectable change in signal was recorded by the inspection tool. Note that defects where the inspection signal may have been tainted by lying too close to a strongly scattering native defect, represented by open diamonds in Fig. 7, are excluded from this comparison. We also note that the Lasertec inspection tool is a high-throughput inspection system that operates forty to several thousand times faster than the actinic inspection system, and that higher sensitivity and/or selectivity may be possible at lower, non-commercial throughput speeds.

Both plots shows that there is a broad correlation between non-actinic and actinic signal strengths, however a significant number of points deviate from this trend. Indeed, for both the brightfield and darkfield comparisons, no more than a rough tend line can be established through the data with significant variability either side of the trend line. Of particular interest are the significant number of defects, plotted along the horizontal axis, that were detected by the actinic tool but not seen in the non-actinic inspection. While this is the subject of ongoing research, we attribute the detection differences to the different wavelength response at 13.4-nm and 488-nm.

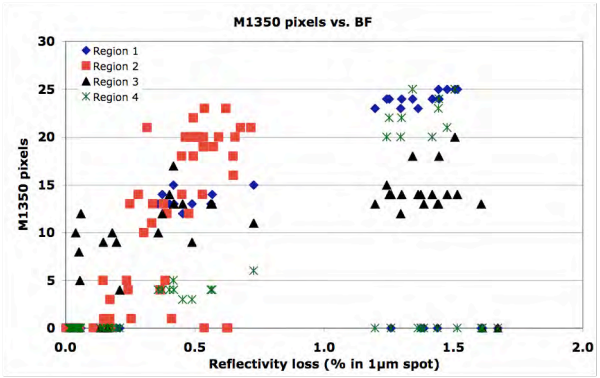

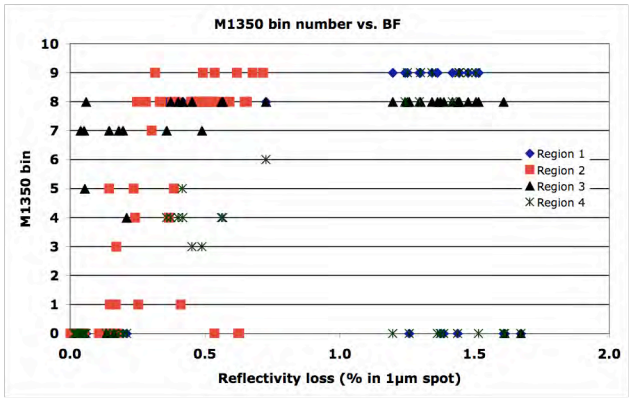

Fig. 8. Scatter plot showing the correlation between actinic brightfield signal (horizontal axis) and Lasertec units of pixel and bin count (vertical axes). Defects plotted on the horizontal axis produced an actinic signal, but were not detected by the non-actinic inspection.

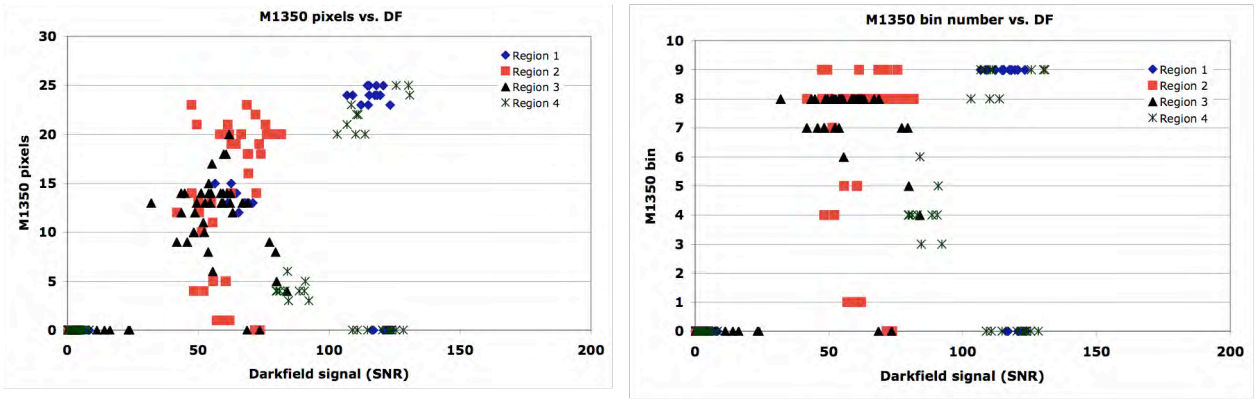

Fig. 9. Scatter plot showing the correlation between actinic darkfield signal (horizontal axis) and Lasertec units of pixel and bin count (vertical axes). Defects plotted on the horizontal axis produced an actinic signal, but were not detected by the non-actinic inspection.

7 Comparison with printing in a micro-exposure tool

The inspection tools' ability to predict open-field defect printability is a primary measure of their value and success. To validate the inspection results, printing tests of the programmed defect array were conducted using the Berkeley Micro-Exposure Tool (MET)[5]. The defect field was printed through varying focus and dose, and SEM inspection was used to determine the *printability* of each defect. Defect printability measurements are compared to both non-actinic and actinic inspection results forming a three-way defect printability and inspection sensitivity cross-comparison. Fig. 10 shows a comparison of actinic brightfield and darkfield signals versus printability, and M1350 inspection results versus defect printability.

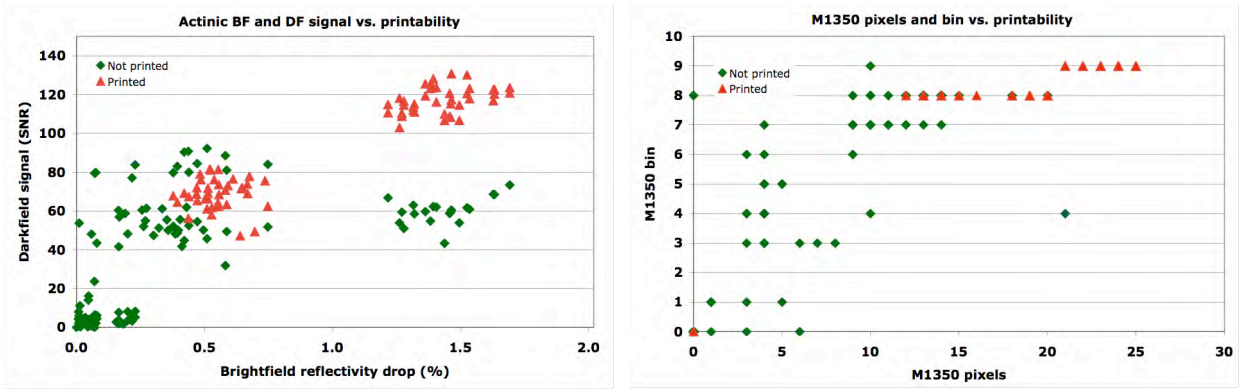

Fig. 10. Scatter plots showing the correlation between actinic brightfield and darkfield signal measured in the LBL inspection system and printability **(a)** and Lasertec units of pixel and bin count versus printability **(b)**. Defects are grouped according to whether the defects were printable or unprintable in MET micro-exposures. Note in particular the cluster of printable defects located at (0,0) in the M1350 scan data – according to our correlations, these defects printed but were not detected by M1350 non-actinic inspection.

As with the comparisons shown above, the actinic brightfield/darkfield plot shows a significant amount of scatter in the data. Although a general trend towards higher signal is seen for printable defects, the scatter in the data is significant with no clear separation between printable and unprintable defects according to any single parameter observed in the data. In particular, selectivity between printable and unprintable defects appears difficult based on this data alone. For M1350 inspection, there appears to be greater separation between printable and unprintable defects, except for a cluster of defects located at (0,0) which were printable but were not present in the Lasertec inspection file. We note again, however, that for the Lasertec inspection system, the defect detection threshold is set

high (approximately 7σ) to avoid false positives within the measurement of the entire quality area of a mask under inspection, and that this choice of detection threshold represents may mean that some of the programmed defect pits may not have been reported as defects even though a detectable change in signal was recorded by the inspection tool. Notwithstanding this observation, the failure to detect significant numbers of printable defects is clearly of concern and needs further investigation, and stands in contrast to the actinic inspection result where a significant change in both brightfield and darkfield signal was measured for all printable defects.

8 Conclusions

We have performed cross-comparisons of actinic and non-actinic inspection of multilayer defects nucleated by programmed substrate pit defects of varying sizes using both at-wavelength and commercial laser-based inspection systems, and we have compared the inspection results to resist printing in the Berkeley MET micro-exposure tool.

A general correlation was observed between signal levels in both the actinic and non-actinic inspection tools for specific defects, however there is a significant degree of data scatter that degrades the correlation. This scatter in the data may be caused by differences in wavelength response between EUV and 488-nm laser light inspection.

Correlation studies with MET printing results indicate that all printable defects showed significant actinic brightfield and darkfield signal, although selectivity between printable and unprintable defects was not particularly high. M1350 inspection results appeared to be well selected for printable defects for those defects that were actually detected; however, a significant number of printed defects was not detected.

This study was conducted on a field of isolated programmed pit defects and represents one of the first cross-comparison measurements available between printing, actinic, and non-actinic inspection. Currently, there is great concern about the detrimental effects of proximity defects, locate within patterned regions. Accordingly, we have prepared a programmed defect mask with both isolated and proximity programmed pit defects programmed defects for a second round of inspection and printability cross-comparisons. The results of this follow-up study will be reported at a subsequent date.

9 References

[1] A.Barty, Y.Liu, E.M.Gullikson, J.S.Taylor and O.Wood, “Actinic inspection of multilayer defects on EUV masks”, (2005) 5751 Proc. SPIE 651

[2] Y.Liu, A.Barty, E.M.Gullikson, J.S.Taylor, J.A.Liddle and O.Wood, “A Dual-Mode Actinic EUV Mask Inspection Tool”, (2005) 5751 Proc. SPIE, 660.

[3] A.Barty, J.S.Taylor, R.Hudyma, E.Spiller, D.W.Sweeney, G.Shelden and J-P Urbach, “Aerial image microscopes for the inspection of defects in EUV masks” (2002) 1889 Proc. SPIE 1073.

[4] "High resolution EUV imaging tools for resist exposure and aerial imaging monitoring", A. Brunton, et. al., Paper 5751-06 presented at Emerging Lithographic Technologies IX, SPIE, San Jose, CA March 1-3, 2005.

[5] P. Naulleau, K. A. Goldberg, J. P. Cain, E. Anderson, P. Denham, K. Jackson, S. Rekawa, F. Salmassi, G. Zhang, "Extreme Ultraviolet Microexposures at the ALS using the 0.3-NA MET Optic," Journal of Vacuum Science and Technology B 22 (6), 2962-65 (2004).

This work was performed under the auspices of the U.S. Department of Energy by the University of California, Lawrence Livermore National Laboratory under Contract No. W-7405-Eng-48.